Semester Project: Variational Monte-Carlo for strongly correlated bosons in continuous space

Giorgio Facelli
giorgio.facelli@epfl.ch

June 9, 2023

Hosting group: CQSL lead by Prof. Giuseppe Carleo
Supervision: Gabriel Pescia

1 Introduction

In recent years, tremendous improvements have been witnessed in the field of Machine Learning (ML) for science applications [1]. Many of these improvements have been triggered by the development of highly flexible and accurate architectures based on Artificial Neural Networks (ANNs) to approximate arbitrary high-dimensional functions, characteristic which gives to ANNs the notorious nickname *universal function approximators*. In particular, in the context of many-body quantum systems, symmetry-aware ANNs allowed the investigation of many-body wavefunctions by restricting considerably the ensemble of possible solutions.
Academic research fields such as condensed matter theory, quantum chemistry and materials science increasingly deal with many-body quantum systems, of which *ab initio* analytical solutions often cannot be found because of their complex interactions. Monte Carlo (MC) methods, at the expense of statistical errors, are good candidates for an exact description of the system. This family of techniques has in fact been shown to be very valuable in studying physical systems [2–6]. One of them is the well-known *Variational Monte Carlo* (VMC), which introduces a variational ansatz that gets iteratively optimized until a minimum is found in energy, and the ground state wavefunction is found. However, recent research on the topics has shown that ANNs represent a promising candidate to solve some of these pressing problems. These methods generally work in conjuction with MC statistical techniques such as VMC.
Variational ansatzes parametrized by ANNs, often called Neural Quantum States (NQSs), can serve as optimal estimators of complicated and highly-entangled wavefunctions. Until now, many efforts have been devoted to study equilibrium and out-of-equilibrium systems with discrete degrees of freedom [7–12]. Quite recently, also early research work has developed state-of-the-art results for continuous-variable systems, both in periodic and non-periodic settings [13–16].
In this study, we implement a NQS architecture inspired from *graph neural networks*, which can efficiently encode relationships in the data, called Message-Passing Neural Networks (MPNNs). We will apply this to study bosonic many-body quantum systems interacting through a gaussian core potential and with periodic boundary conditions (PBCs). In the Methods section we present the

theoretical framework which allows to model the system, as well as the architecture employed as the ground-state variational ansatz. In the Results section, we first benchmark some important hyperparameters related to the ansatz. We then move on to study the physical properties of the system, where we show the presence of two distinct phases of matter. We then discuss the main results presented and finally draw the conclusions of this study.

2 Methods

2.1 Variational Monte carlo

The core idea of VMC is to exploit the *variational principle* to study the low-energy properties of many-body quantum systems. The principle states that the energy of a physical system is minimized by the ground state eigenvector $|\Psi_0\rangle$ associated to the Hamiltonian of the system:

$$|\Psi_0\rangle = \underset{|\Psi\rangle}{\operatorname{argmin}} \left[\frac{\langle\Psi|\hat{H}|\Psi\rangle}{\langle\Psi|\Psi\rangle} \right] \tag{1}$$

To do this, in VMC a variational ansatz $|\Psi(\boldsymbol{\theta})\rangle$ is used, and its parameters $\boldsymbol{\theta}$ are iteratively optimized so as to reach the minimum in energy. Hence, the estimator of the ground-state eigenvector will be $|\Psi(\boldsymbol{\theta}_0)\rangle$ such that $\boldsymbol{\theta}_0$ satisfies:

$$\boldsymbol{\theta_0} = \underset{\boldsymbol{\theta}}{\operatorname{argmin}} \left[\frac{\langle\Psi(\boldsymbol{\theta})|\hat{H}|\Psi(\boldsymbol{\theta})\rangle}{\langle\Psi(\boldsymbol{\theta})|\Psi(\boldsymbol{\theta})\rangle} \right] \tag{2}$$

This allows the variational ansatz to approximate the ground-state eigenvector, with which we can gain insight to the physical properties of the system.

2.2 Estimation of observables

Expectation values of observables cannot in general be computed efficiently. In fact, for $\langle\hat{O}\rangle = \langle\Psi|\hat{O}|\Psi\rangle \,/\, \langle\Psi|\Psi\rangle$, computing the normalization term is in general unfeasible. However, using MC integration, we can efficiently approximate most physical observables by a statistical average over its so-called *local* observable:

$$\begin{aligned} \frac{\langle\Psi|\hat{O}|\Psi\rangle}{\langle\Psi|\Psi\rangle} &= \frac{\int d\boldsymbol{x} \int d\boldsymbol{x'} \Psi(\boldsymbol{x})^* \langle\boldsymbol{x}|\hat{O}|\boldsymbol{x'}\rangle \Psi(\boldsymbol{x'})}{\int d\boldsymbol{x} |\Psi(\boldsymbol{x})|^2} = \\ &= \frac{\int d\boldsymbol{x} |\Psi(\boldsymbol{x})|^2 O_{\mathsf{loc}}(\boldsymbol{x})}{\int d\boldsymbol{x} |\Psi(\boldsymbol{x})|^2} = \mathbb{E}_{\Pi(\boldsymbol{x})}\Big[O_{\mathsf{loc}}(\boldsymbol{x})\Big] \end{aligned} \tag{3}$$

where we define $O_{\mathsf{loc}}(\boldsymbol{x}) = \int d\boldsymbol{x'} O_{\boldsymbol{x}\boldsymbol{x'}} \frac{\Psi(\boldsymbol{x'})}{\Psi(\boldsymbol{x})}$ (and $O_{\boldsymbol{x}\boldsymbol{x'}} = \langle\boldsymbol{x}|\hat{O}|\boldsymbol{x'}\rangle$) and the expectation value after the last equality in Eq. (3) is over the probability ditribution $\Pi(\boldsymbol{x}) = \frac{|\Psi(\boldsymbol{x})|^2}{\int d\boldsymbol{y} |\Psi(\boldsymbol{y})|^2}$. Finally, by sampling

a large enough set of samples $\{\boldsymbol{x}^{(i)}\}_{i=1}^{M}$ from $\Pi(\boldsymbol{x})$, one can approximate the observable:

$$\langle \hat{O} \rangle = \frac{1}{M} \sum_{i=1}^{M} O_{\text{loc}}(\boldsymbol{x}^{(i)}) \tag{4}$$

The standard procedure of VMC is then to sample positions from the distribution given by the variational ansatz, estimate the mean energy and its gradient and then optimize the parameters in the direction of steepest descent, with the goal to minimize the mean energy. Many techniques can be used to generate a set of samples. In this work, we use the very well-known Metropolis-Hastings algorithm.

2.3 Implementation of a periodic system

Periodic boundary conditions (PBCs) allow to access the bulk properties of extended systems. To be able to include PBCs in a given system, one must ensure that the wavefunction be invariant under translation of a single-particle position by a quantity corresponding to the simulation lattice vectors. $\boldsymbol{x}_i \leftrightarrow \boldsymbol{x}_i + \boldsymbol{L} \cdot \boldsymbol{e}_k$ where $\boldsymbol{x}_i \in \mathbb{R}^d$ is the position of one particle in d spatial dimensions, $\boldsymbol{L}$ is the simulation box size and $\boldsymbol{e}_k$ an arbitrary basis vector of the simulation cell. In order to ensure this condition, the particle positions are mapped into quasi-particle positions as follows:

$$\boldsymbol{x}_i \longmapsto \boldsymbol{r}_i = \left(\sin\left(\frac{2\pi}{\boldsymbol{L}}\boldsymbol{x}_i\right), \cos\left(\frac{2\pi}{\boldsymbol{L}}\boldsymbol{x}_i\right) \right) \tag{5}$$

where $\sin(\frac{2\pi}{\boldsymbol{L}}\boldsymbol{x}_i) = (\sin(\frac{2\pi}{L_1}x_{i,1}), \ldots, \sin(\frac{2\pi}{L_d}x_{i,d}))$. Thus, the transformed position space will double in dimensionality, namely $\boldsymbol{r}_i \in \mathbb{R}^{2d}$. Similarly, one needs to respect the intrinsic periodicity of the system also when computing the inter-particle distances. Hence, in the variational ansatz we will consider a continuous version (for differentiation purposes) of the periodic inter-particle distance defined by $d_{\sin}(i,j) = \|\sin\left(\frac{\pi}{\boldsymbol{L}}\boldsymbol{x}_{ij}\right)\|$, where $\boldsymbol{x}_{ij} = \boldsymbol{x}_{\boldsymbol{i}} - \boldsymbol{x}_{\boldsymbol{j}}$. Finally, to compute the euclidean distance between two particles, respecting also the PBCs, we use the *minum image* convention:

$$d(i,j) = \left\| \boldsymbol{x}_i - \boldsymbol{x}_j - \boldsymbol{L} \left\lfloor \frac{\boldsymbol{x}_i - \boldsymbol{x}_j}{\boldsymbol{L}} \right\rceil \right\| \tag{6}$$

2.4 Gaussian cores

In this study, we consider a 2D system of Bose particles of spin zero interacting via a repulsive Gaussian-core potential, and in a simulation cell with with PBCs. The Hamiltonian takes the following form:

$$H = T + V = -\frac{\hbar^2}{2m} \sum_{i=1}^{N} \vec{\nabla}_i^2 + \varepsilon \sum_{i<j}^{N} \exp\left(-\frac{d(i,j)^2}{2\sigma^2}\right) \tag{7}$$

Where T and V are the kinetic and potential energy respectively, $d(i,j)$ is the minimum image distance between two particles and ε, σ are two constants. This can be written in a more compact

form by normalizing the particle positions by σ^2 and defining the quantum coupling constant $\Lambda = \frac{\hbar^2}{m\varepsilon\sigma^2}$:

$$H = -\frac{\Lambda}{2}\sum_{i=1}^{N}\vec{\nabla}_i^2 + \sum_{i<j}^{N}\exp\left(-\frac{d(i,j)^2}{2}\right) \tag{8}$$

Previous studies have shown that this system exhibits superfluid and crystalline quantum phases of matter depending on the quantum coupling constant Λ and the density $\rho = \frac{N}{L^2}$ (or equivalently the average inter-particle distance $r_s = (\rho\sigma^2)^{-1/2}$) [6, 13]. Here, we will investigate these phenomena by means of the MPNN architecture as described in the next section.

2.5 Message-passing Neural Networks

We propose here to use, as a variational ansatz, a family of graph neural networks (GNNs) known as message-passing neural networks (MPNNs). Their structure is schematically represented by a composition of graphs, such as the one depicted in Fig. 1. These architectures have been shown to be well suited in processing data that can be represented as graphs [17, 18]. In fact, their structure can encode information specific to each component in what are called *nodes*, and information about their relationship, in what are known as *edges*. In our context, information about the inter-particle distances is relevant in determining the spatial structure of the system. Hence, we will use the the edges to encode information about their interactions, and nodes to encode information about their positions. Briefly, for a MPNN with $\mathcal{N}$ graphs, μ-th graph will have the following nodes and edges:

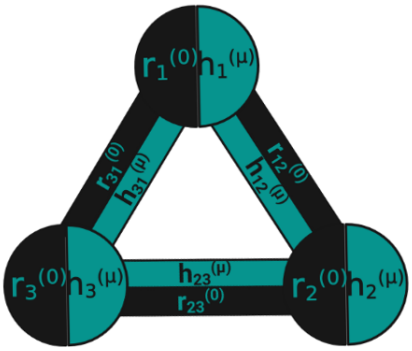

Figure 1: Schematic representation of the μ-th graph of a MPNN. In this case, three input coordinates $r_i^{(0)}$ generate three sets of distances $r_{ij}^{(0)}$, hidden nodes $h_i^{(\mu)}$ and hidden edges $h_{ij}^{(\mu)}$.

$$\boldsymbol{n}_i^{(\mu)} = \left(\boldsymbol{r}_i, \boldsymbol{h}_i^{(\mu)}\right), \quad \boldsymbol{e}_{ij}^{(\mu)} = \left(\boldsymbol{r}_{ij}, d_{\sin}(i,j), \boldsymbol{h}_{ij}^{(\mu)}\right) \tag{9}$$

where $\boldsymbol{r}_i$ are the periodic quasi-particle coordinates introduced in section 2.3. These definitions include $\boldsymbol{h}_i^{(\mu)}$ and $\boldsymbol{h}_{ij}^{(\mu)}$, known as *hidden* nodes and edges, respectively, and defined as:

$$\boldsymbol{h}_i^{(\mu)} = \boldsymbol{f}\left(\boldsymbol{n}_i^{(\mu-1)}, \sum_{i\neq j}\boldsymbol{m}_{ij}^{(\mu)}\right), \quad \boldsymbol{h}_{ij}^{(\mu)} = \boldsymbol{g}\left(\boldsymbol{e}_{ij}^{(\mu-1)}, \boldsymbol{m}_{ij}^{(\mu)}\right) \tag{10}$$

where $\boldsymbol{m}_{ij}^{(\mu)} = \phi\left(\boldsymbol{e}_{ij}^{(\mu-1)}\right)$. The functions $\boldsymbol{f}, \boldsymbol{g}, \boldsymbol{\phi}$ are multi-layer perceptrons (MLPs). For the purpose of this study, we will always take the same activation function GELU$(\cdot)$ for all MLPs. Invariance under exchange of particles is a native property in wavefunctions describing bosonic systems. This translates to having a permutation-equivariant MPNN, which is ensured by taking the same hidden nodes and edges for all particles. Hence, we construct a variational ansatz $\Psi_{\boldsymbol{\theta}}$ by transforming the input coordinates into backflow coordinates $\tilde{\boldsymbol{x}}_i = \text{MPNN}(\boldsymbol{x})_i = \boldsymbol{n}_i^{(\mathcal{N})}$ and applying a final MLP $\boldsymbol{\rho}$:

$$\log[\Psi_{\boldsymbol{\theta}}(\boldsymbol{x})] = \sum_i \boldsymbol{\rho}(\tilde{\boldsymbol{x}}_i) = \sum_i \boldsymbol{\rho}(\text{MPNN}(\boldsymbol{x})_i) \tag{11}$$

where $\boldsymbol{x} = (\boldsymbol{x}_1, ..., \boldsymbol{x}_N)$ are the original single-particle coordinates.

2.6 LayerNorm

To improve training we apply the so-called *LayerNorm* (LN). This feature proposes to re-center and normalize the nodes of a neural network layer after application of the activation function. If $\boldsymbol{y}$ is the output of a given layer with width W, then LN will induce the following transformation:

$$\boldsymbol{y'} = \frac{\boldsymbol{y} - \mu}{\sigma}, \quad \mu = \frac{1}{W}\sum_{i=1}^{W} y_i, \quad \sigma = \sqrt{\frac{1}{W}\sum_{i=1}^{W}(y_i - \mu)^2} \tag{12}$$

This normalization has been shown to improve training for neural network models [19], with faster overall convergence. In a similar way, we will study the efficiency of this method on our optimizations and evaluate if it should be included in the definition of our MPNN model.

2.7 Radial correlation function

An important physical quantity to study the spatial structure among the simulated particles is the two-body radial correlation function. In short, this function tells us how likely a particle is going to be sitting at a distance $\boldsymbol{r}$ from a reference particle. It is defined as:

$$g_2(\boldsymbol{r}) = \frac{1}{N\rho}\langle\sum_{i\neq j}^{N}\delta(\boldsymbol{r} - \boldsymbol{r}_{ij})\rangle \tag{13}$$

where $\delta(\cdot)$ is the delta function. The spherically averaged distribution is given by:

$$g_2(r) = \frac{1}{N\rho}\frac{1}{4\pi r^2}\langle\sum_{i\neq j}^{N}\delta(r - r_{ij})\rangle \tag{14}$$

This is instead called the pair correlation function. Both the radial and pair correlation function will give us insight on the emergent physical structure of a system.

2.8 Structure factor

Another important physical quantity is the structure factor, useful in determining the scattering properties of incident radiations on a material, which can be used to infer the atomic arrangement

of a material. It relates the intensity of diffracted light as a function of the scattering vector $\boldsymbol{q} = \boldsymbol{k}_0 - \boldsymbol{k}_f$ (where $\boldsymbol{k}_0$ is the initial wavevector and $\boldsymbol{k}_f$ the final one). In mathematical terms:

$$S(\boldsymbol{q}) = \frac{1}{N} \left| \langle \sum_{i=1}^{N} e^{-i\boldsymbol{q}\cdot\boldsymbol{r}_i} \rangle \right|^2 \tag{15}$$

where again $\boldsymbol{r}_i$ are the single-particle positions. In mathematical terms, the structure factor corresponds to the Fourier transform of the radial distribution function defined in Eq. (13):

$$\begin{aligned} S(\boldsymbol{q}) = \frac{1}{N} \left| \langle \sum_{i=1}^{N} e^{-i\boldsymbol{q}\cdot\boldsymbol{r}_i} \rangle \right|^2 = \frac{1}{N} \langle \sum_{i,j}^{N} e^{-i\boldsymbol{q}\cdot(\boldsymbol{r}_i - \boldsymbol{r}_j)} \rangle = 1 + \frac{1}{N} \langle \sum_{i \neq j} e^{-i\boldsymbol{q}(\boldsymbol{r}_i - \boldsymbol{r}_j)} \rangle = \\ = 1 + \frac{1}{N} \langle \int d\boldsymbol{r} e^{-i\boldsymbol{q}\boldsymbol{r}} \sum_{i \neq j} \delta(\boldsymbol{r} - \boldsymbol{r}_i - \boldsymbol{r}_j) \rangle = 1 + \rho \int d\boldsymbol{r} e^{-i\boldsymbol{q}\boldsymbol{r}} g_2(\boldsymbol{r}) \end{aligned} \tag{16}$$

where the last equality becomes straightforward by identifying $\boldsymbol{r}_i - \boldsymbol{r}_j = \boldsymbol{r}_{ij}$.

2.9 About the code

The code has been entirely implemented on Python, with extensive use of libraries such as JAX, which allows automatic differentiation and just-in-time compilation, and Flax, a machine-learning library built specifically for JAX. Finally, the VMC approach, which includes sampling and optimization, is entirely automated through the NetKet library [20].

3 Results

The results shown consider a system of $N = 16$ bosons interacting via a gaussian-core potential. Unless said otherwise, the system is in a square simulation box and we set the quantum coupling constant $\Lambda = 1/30$. All simulations are conducted making use of *stochastic gradient descent* and *stochastic reconfiguration*. The latter computes the variational ansatz advanced infinitesimally in imaginary time, in order to maximize its overlap with the given variational ansatz at each optimization step. This step improves overall convergence, since an imaginary-evolved ansatz naturally tends to the ground state. In a first moment, we focus on the computational aspects of the architeture and its performance. Secondly, we investigate the physical aspects of the system, in particular phases of matter and ground-state properties.

3.1 NQS architecture performances

MPNN architecture

Important features of the architecture are studied and their impact on the performance is investigated. In particular, we relate how the size of the architecture, and hence the number of parameters

encoding the wavefunction, influences the precision of the ground-state approximation. Considering the system at $\rho = 1/9$, Fig. 2a shows four energy optimizations, each with a different number of consecutive graphs, and similarly Fig. 2b with differing number of hidden layers in the $\boldsymbol{f}, \boldsymbol{g}, \boldsymbol{\phi}, \boldsymbol{\rho}$ MLPs as described in section 2.5. In the first case, the number of graphs has a direct impact on the outcome of the simulation, resulting in increasingly better estimates of the ground-state energy. In the latter case, however, a high number of layers does not imply better performances. In Tab. 1 we report the values of final ground-state energies estimated during the optimizations reported in Figs. 2a, 2b, where we note that the the number of graphs has a greater impact on the precision of the system'e energy.

Table 1: Ground-state energy per particle for $N = 16$ at density $\rho = 1/9$ in 2D interacting through a gaussian core potential, for different number of graphs and different number of hidden layers.

n°	graphs	hidden layers
1	0.08515	0.08516
2	0.08471	0.08487
3	0.08468	0.08471
4	0.08457	0.08486

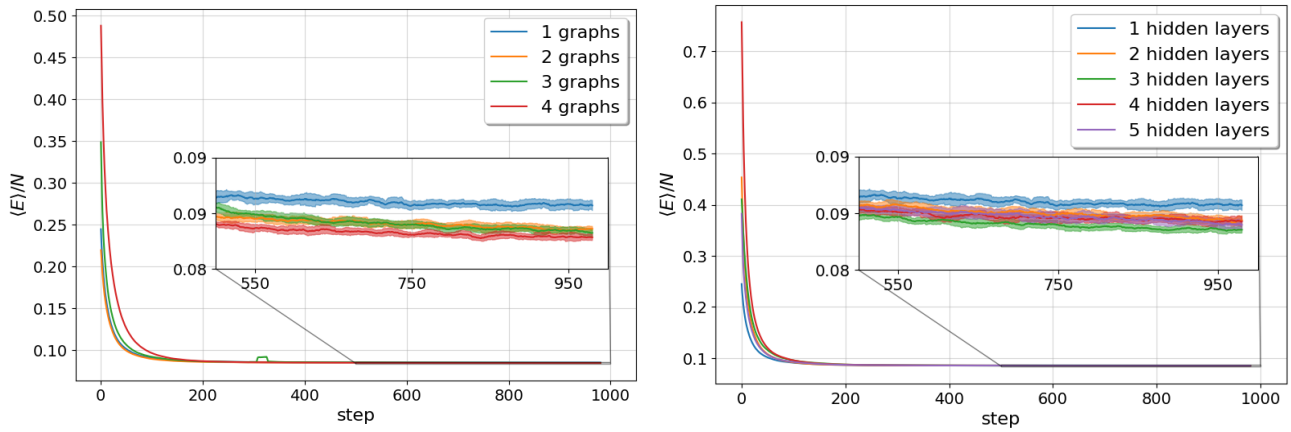

(a) **(b)**

Figure 2: Comparison of energy optimizations for $N = 16$ gaussian cores in 2D at $\rho = 1/9$. **(a)** Varying the number of graphs: the curves indicate that a better perfomance can be accessed with a greater number of graphs. **(b)** Varying the number of hidden layers: here an increase in the variational parameters does not always increase accuracy (optimization with 3 hidden layers outperforms optimizations with 4 or 5).

LayerNorm

Here, we benchmark the performance of the additional normalization step LayerNorm as presented in section 2.6. Multiple optimizations show that indeed LN is able to reach faster and precise convergence. In Tab. 2, the energies per particle show that this method is able to reach lower values for the ground-state energies, yielding therefore more accurate results. Given the clear advantage of the LayerNorm additional step, the next results will make use of it.

Table 2: Energy per particle for $\rho = 4/9, 1/9$ with and without applying LN after each activation layer in the MPNN architecture.

	No LN	LN
$\rho = 4/9$	1.00498	1.00403
$\rho = 1/9$	0.08534	0.08515

3.2 Quantum phases of matter

To better understand the quantum phases of matter that the system has, we study the impact of the system density on the pair correlation function, defined as in Eq. (14), which gives us insight on how the position of one particle correlates to another one. To witness the structural changes, we take inspiration from the ground-state phase diagram in Ref. [6] and consider $\rho = 4/9, 1/9, 1/16$. Results are showed in Fig. 3, revealing two different phases of matter. In a first moment the high density yields a supefluid phase of matter (blue plot in the figure). At intermediate dentities, instead, the potential energy becomes more important and triangular crystalline phase arises. This is visible in green and especially orange plots, where their periodicity in the radial correlation function also at large distances arises because of long range order, which is indication of crystal structure.

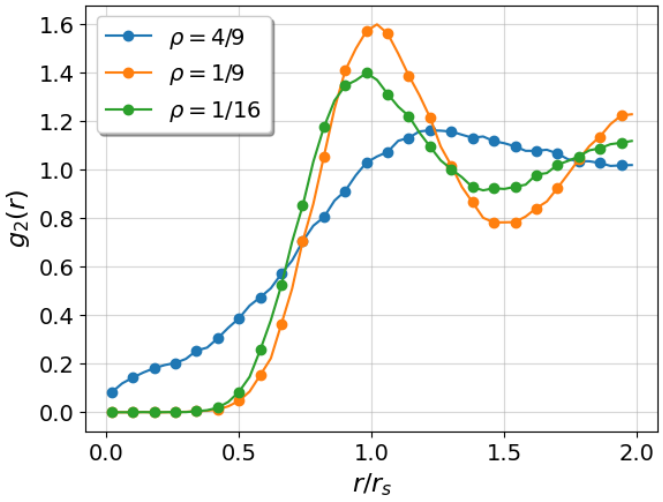

Figure 3: Ground-state pair correlation function as a function of the normalized distance for $N = 16$ gaussian cores in 2D at average densities of $4/9$ (blue), $1/9$ (orange), $1/16$ (green). The plots indicate an initial liquid phase at high densitites with a non-zero value at the origin. At intermediate densities, a crystalline phase appears, showing a vanishing value of $g_2(r)$ at low distances and a periodic behaviour at higher ones. Then, the oscillating structure weakens again for low densities. The final ground-state energy-per-particle are $E/N = 1.00498, 0.08533, 0.02440$ respectively.

3.3 Geometry of the simulation box and its impact on the system

We now look at the influence of the system's geometry on the crystalline structure of the system. In particular, by changing the ratio of the simulation box by a factor a, yielding dimensions $\boldsymbol{L} = (L\sqrt{a}, L/\sqrt{a})$, we can gain insight on the impact that the aspect ratio has. In this section, we

consider $\Lambda = 1/100$ and $\rho = 1/9$. This ensures that the system is well within the boundaries of the crystalline phase. Firstly, Fig. 4a reports the ground-state energy as a function of the factor a, revealing a local minimum at $a = 2/\sqrt{3}$. This is in fact the most natural configuration of the system, since the ratio is in accordance with that of the primitive lattice vectors, leading to a relaxation in energy. The aspect ratio a has impact on the crystalline structure as well, increasing the magnitude of damping in the periodicity of the pair correlation function (see Fig. 4b).

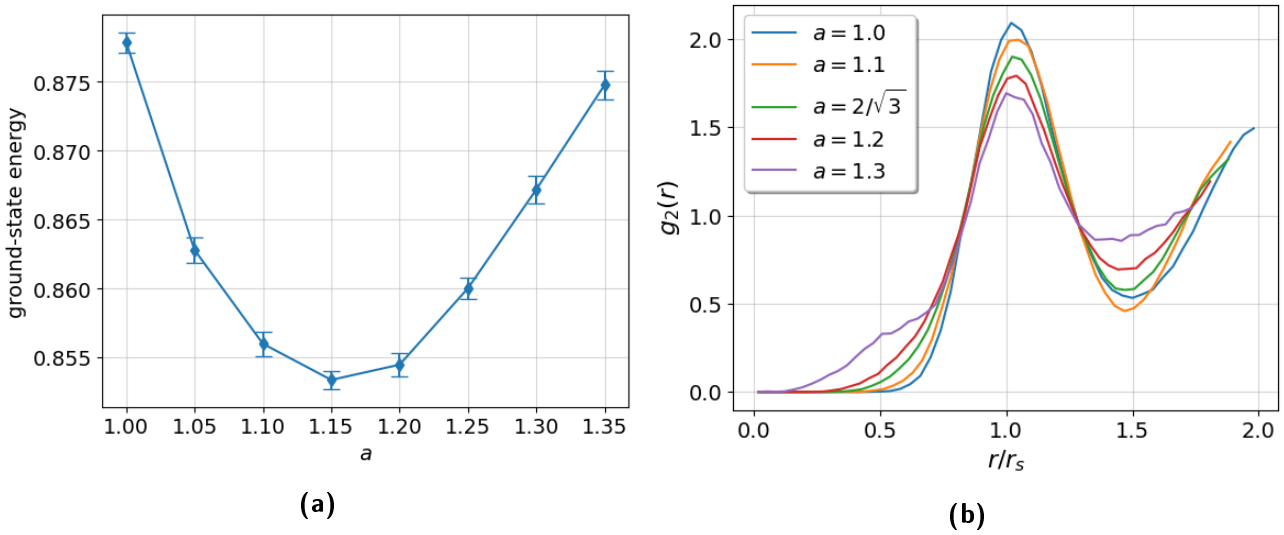

Figure 4: System of $N = 16$ particles in 2D at $\rho = 1/9$, interacting though a gaussian-core potential **(a)** Total ground-state energy as a function of the aspect ratio a. A minimum is found in the vicinity of $a = \sqrt{2}/3$. All error bars are all 1σ away from the mean. **(b)** Pair correlation function against the distance r/r_s, for different values of a. A dampening effect is seen as a is increased to higher values.

To gain a deeper understanding of the self-assembling arrangement of the system and the respective localization of its consituents, we also plot in Figs. 5a, 5b the radial distribution function (Eq. (13)) as well as the square root of the structure factor (Eq. (15)) for different values of the aspect ratio, namely $a = 1, 1.1, \sqrt{2}/3, 1.3$. In both sets of plots, the patterns indicate that for $a = 2/\sqrt{3}$ the particles are in a more localized arrangement with respect to the other ones. In fact, for a simple square box ($a = 1$), we only have a radial-dependent correlation, which breaks for $a > 1$ and we start to see well-localized clusters of high-probability occupation. The same can be said in regards to the structure factor, where $a = 2/\sqrt{3}, 1.3$ are the ratios in which $S(\boldsymbol{q})$ is most localized.

4 Discussion

In this study, the MPNN-based architecture has been put to the test by studying the ground-state properties of a 2D system of $N = 16$ bosons interacting through a gaussian-core potential. We have shown good estimations of the ground-state energy, in line with results of similar systems in Ref. [13]. The approximations can be further improved by encoding the variational ansatz into a greater number of parameters. This can be achieved by tuning hyperparameters of the architecture such as number of graphs, number of layers and width of the layers. In particular, we have seen that increasing the number of graphs is the most effective hyperparameter, as it consistently improves

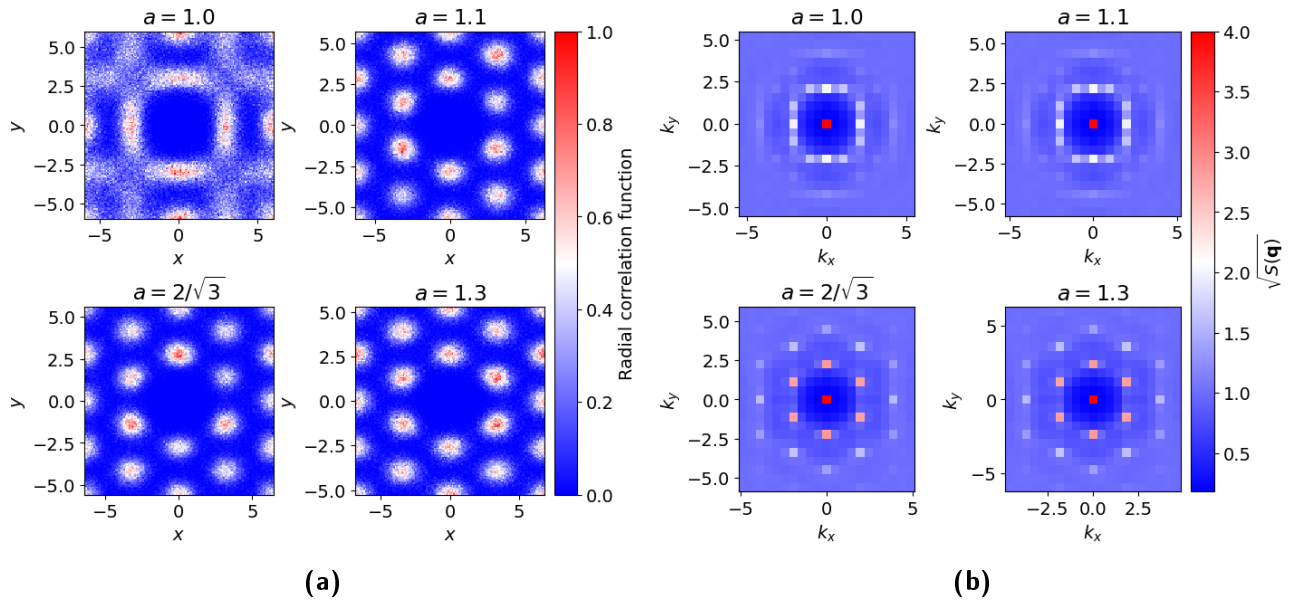

Figure 5: System of $N = 16$ particles at $\rho = 1/9$ in 2D iteracting through a gaussian core potential. **(a)** Radial correlation function as a function of spatial coordinates $\boldsymbol{r} = (x, y)$, for different values of the system's aspect ratio. **(b)** Square root of the structure factor as a function of the wavevector $\boldsymbol{q} = (k_x, k_y)$, for different values of the system's aspect ratio. The $(\cdot)^{\frac{1}{2}}$ rescaling allows to make the patterns more visible for each plot.

the energy estimation. Instead, the number of hidden layers does not have a direct impact on the perfomance. This is very likely due to a redundancy of the parameters, which does not always guarantee an improvement in the accuracy. Moreover, the variational ansatz has proven to be versatile and able to encode the ground-state wavefunction in all scenarios which we considered, without any initial bias on the expected structure of the system. This allowed us also to study its physical properties, where it was shown that the system presents two different phases of matters, superfluid and crystalline, depending on the density. For high values of ρ the dynamics of the system is completely dominated by quantum delocalization given the high-energy interactions. For low values, the system is instead relaxed as the potential energy is much smaller than the energy of zero point fluctuations, and therefore the system cannot self-assemble into a crystal-like structure. At intermediate values of the density ($\rho = 1/9$), there is instead good balance between the interaction and kinetic energy, which allows the system to organize into a triangular crystal phase. Given that the solid phase has a triangular-like unit cell, we further studied the properties of the system for different aspect ratios a of the simulation box. A relaxation in energy is seen until $a = 2/\sqrt{3}$ (see Fig. 4a). This is because it is the same aspect ratio as the primitive lattice vectors, and thus the box will be able to host more naturally the crystallization of the system. As a consequence, the radial correlation function in Fig. 5a has more localized clusters of high-probability occupation, which represent the more robust crystalline structure of the system. Similarly, the structure factor (Fig. 5b) has a greater quantization of wavevectors $\boldsymbol{q}$ allowed for scattering, reflecting the fact that the real-space lattice has a well-defined structure. It would be of interest to conduct the same studies on a larger system, and understand which results generalize well and which ones instead are caused by finite size effects.

5 Conclusions

In this study we presented novel state-of-the-art NQS architectures based on GNNs to study bosonic particles under a gaussian core interaction in a periodic system. The perfomance was investigated by varying the hyperparameters of the MPNN model, such as number of graphs and hidden layers. Its accuracy shows that indeed the model is able capture the behaviour of highly-correlated quantum systems. We then studied the ground-state properties, with particular emphasis on its phases of matter and the corresponding emergent structures. It was found that the system has a crystalline and superfluid phase, the latter emerging at higher or lower densities. The results were also in good agreement with similar studies that considered larger system sizes, such as Refs. [6, 13]. Finally, just like done in Ref. [14], it would be of great interest to extend such architectures to fermionic systems and test its performance when antisymmetric wavefunctions are considered. These advanced computational techniques pave the way to further research in the context of many-body quantum systems in continuous space, essential in disciplines such as quantum chemistry and materials science.

References

[1] Giuseppe Carleo et al. "Machine learning and the physical sciences". In: *Rev. Mod. Phys.* 91 (4 Dec. 2019), p. 045002. DOI: 10.1103/RevModPhys.91.045002. URL: https://link.aps.org/doi/10.1103/RevModPhys.91.045002.

[2] W. L. McMillan. "Ground State of Liquid He^4". In: *Phys. Rev.* 138 (2A Apr. 1965), A442–A451. DOI: 10.1103/PhysRev.138.A442. URL: https://link.aps.org/doi/10.1103/PhysRev.138.A442.

[3] Daniel Schiff and Loup Verlet. "Ground State of Liquid Helium-4 and Helium-3". In: *Phys. Rev.* 160 (1 Aug. 1967), pp. 208–218. DOI: 10.1103/PhysRev.160.208. URL: https://link.aps.org/doi/10.1103/PhysRev.160.208.

[4] Tobias Dornheim et al. "Ab Initio Quantum Monte Carlo Simulation of the Warm Dense Electron Gas in the Thermodynamic Limit". In: *Phys. Rev. Lett.* 117 (15 Oct. 2016), p. 156403. DOI: 10.1103/PhysRevLett.117.156403. URL: https://link.aps.org/doi/10.1103/PhysRevLett.117.156403.

[5] W. R. Magro and D. M. Ceperley. "Ground state of two-dimensional Yukawa bosons: Applications to vortex melting". In: *Phys. Rev. B* 48 (1 July 1993), pp. 411–417. DOI: 10.1103/PhysRevB.48.411. URL: https://link.aps.org/doi/10.1103/PhysRevB.48.411.

[6] Peter Kroiss, Massimo Boninsegni, and Lode Pollet. "Ground-state phase diagram of Gaussian-core bosons in two dimensions". In: *Phys. Rev. B* 93 (17 May 2016), p. 174520. DOI: 10.1103/PhysRevB.93.174520. URL: https://link.aps.org/doi/10.1103/PhysRevB.93.174520.

[7] Giuseppe Carleo and Matthias Troyer. "Solving the quantum many-body problem with artificial neural networks". In: *Science* 355.6325 (2017), pp. 602–606. DOI: 10.1126/science.aag2302. eprint: https://www.science.org/doi/pdf/10.1126/science.aag2302. URL: https://www.science.org/doi/abs/10.1126/science.aag2302.

[8] Mohamed Hibat-Allah et al. "Recurrent neural network wave functions". In: *Phys. Rev. Res.* 2 (2 June 2020), p. 023358. DOI: 10.1103/PhysRevResearch.2.023358. URL: https://link.aps.org/doi/10.1103/PhysRevResearch.2.023358.

[9] Kenny Choo et al. "Symmetries and Many-Body Excitations with Neural-Network Quantum States". In: *Phys. Rev. Lett.* 121 (16 Oct. 2018), p. 167204. DOI: 10.1103/PhysRevLett.121.167204. URL: https://link.aps.org/doi/10.1103/PhysRevLett.121.167204.

[10] Kenny Choo, Antonio Mezzacapo, and Giuseppe Carleo. "Fermionic neural-network states for ab-initio electronic structure". In: *Nature Communications* 11.1 (May 2020), p. 2368. ISSN: 2041-1723. DOI: 10.1038/s41467-020-15724-9. URL: https://doi.org/10.1038/s41467-020-15724-9.

[11] Stefanie Czischek, Martin Gärttner, and Thomas Gasenzer. "Quenches near Ising quantum criticality as a challenge for artificial neural networks". In: *Phys. Rev. B* 98 (2 July 2018), p. 024311. DOI: 10.1103/PhysRevB.98.024311. URL: https://link.aps.org/doi/10.1103/PhysRevB.98.024311.

[12] Nobuyuki Yoshioka, Wataru Mizukami, and Franco Nori. "Solving quasiparticle band spectra of real solids using neural-network quantum states". In: *Communications Physics* 4.1 (May 2021), p. 106. ISSN: 2399-3650. DOI: 10.1038/s42005-021-00609-0. URL: https://doi.org/10.1038/s42005-021-00609-0.

[13] Gabriel Pescia et al. "Neural-network quantum states for periodic systems in continuous space". In: *Phys. Rev. Res.* 4 (2 May 2022), p. 023138. DOI: 10.1103/PhysRevResearch.4.023138. URL: https://link.aps.org/doi/10.1103/PhysRevResearch.4.023138.

[14] Gabriel Pescia et al. *Message-Passing Neural Quantum States for the Homogeneous Electron Gas*. 2023. arXiv: 2305.07240 [quant-ph].

[15] David Pfau et al. "Ab initio solution of the many-electron Schrödinger equation with deep neural networks". In: *Phys. Rev. Res.* 2 (3 Sept. 2020), p. 033429. DOI: 10.1103/PhysRevResearch.2.033429. URL: https://link.aps.org/doi/10.1103/PhysRevResearch.2.033429.

[16] Jan Hermann, Zeno Schätzle, and Frank Noé. "Deep-neural-network solution of the electronic Schrödinger equation". In: *Nature Chemistry* 12.10 (Oct. 2020), pp. 891–897. ISSN: 1755-4349. DOI: 10.1038/s41557-020-0544-y. URL: https://doi.org/10.1038/s41557-020-0544-y.

[17] Franco Scarselli et al. "The Graph Neural Network Model". In: *IEEE Transactions on Neural Networks* 20.1 (2009), pp. 61–80. DOI: 10.1109/TNN.2008.2005605.

[18] Alessio Micheli. "Neural Network for Graphs: A Contextual Constructive Approach". In: *IEEE Transactions on Neural Networks* 20.3 (2009), pp. 498–511. DOI: 10.1109/TNN.2008.2010350.

[19] Jingjing Xu et al. *Understanding and Improving Layer Normalization*. 2019. arXiv: 1911.07013 [cs.LG].

[20] Filippo Vicentini et al. "NetKet 3: Machine Learning Toolbox for Many-Body Quantum Systems". In: *SciPost Phys. Codebases* (2022), p. 7. DOI: 10.21468/SciPostPhysCodeb.7. URL: https://scipost.org/10.21468/SciPostPhysCodeb.7.